AGU100 ADVANCING EARTH AND SPACE SCIENCE

JGR

Journal of Geophysical Research: Space Physics

RESEARCH ARTICLE
10.1029/2018JA025332

**Key Points:**
- Equatorial plasma bubbles velocity is derived by cloud motion wind (CMW) technology by tracking a series of successive airglow images
- CMW can obtain the velocity of different parts in EPB
- Results of CMW are compared with STEC data and show a good consistency, but some errors are also discussed

**Correspondence to:**
T. Yu,
yutaommnn@163.com

**Citation:**
Yu, T., Li, M., Xia, C., Zuo, X., Liu, Z., & Zhao, B. (2018). A new method for deriving equatorial plasma bubble velocity by tracing OI 630 nm all-sky images. *Journal of Geophysical Research: Space Physics*, *123*, 9619–9633. https://doi.org/10.1029/2018JA025332

Received 8 FEB 2018
Accepted 21 AUG 2018
Accepted article online 31 AUG 2018
Published online 8 NOV 2018



# A New Method for Deriving Equatorial Plasma Bubble Velocity by Tracing OI 630 nm All-Sky Images

**Tao Yu[1,2], Mingyuan Li[1], Chunliang Xia[1], Xiaomin Zuo[1], Zhizhao Liu[2], and Biqiang Zhao[3,4]**

[1]Hubei Subsurface Multi-scale Imaging Key Laboratory, Institute of Geophysics and Geomatics, China University of Geosciences, Wuhan, China, [2]Department of Land Surveying and Geo-Informatics, The Hong Kong Polytechnic University (PolyU), Kowloon, Hong Kong, [3]Key Laboratory of Earth and Planetary Physics, Institute of Geology and Geophysics, Chinese Academy of Sciences, Beijing, China, [4]College of Earth Sciences, University of the Chinese Academy of Sciences, Beijing, China

**Abstract** A new method for estimating the equatorial plasma bubbles (EPBs) motions from airglow emission all-sky images is presented in this paper. This method, which is called *cloud motion wind* (CMW) and widely used in satellite observation of wind, could reasonably derive zonal and meridional velocity vectors of EPBs drift by tracking a series of successive airglow images. Airglow emission images data are available from all-sky airglow camera in Hainan Fuke (19.5°N, 109.2°E) supported by China Meridional Project, which can receive the 630.0 nm emission from ionosphere *F* region at low latitudes to observe plasma bubbles. A series of pretreatment technology is utilized to preprocess the raw observation. Then the regions of plasma bubble extracted from the images are divided into several small tracing windows, and each tracing window can find a target window in the searching area in following image, which is considered as the position tracing window moved to. According to this, velocity of each tracing window was calculated by CMW. The maximum correlation coefficient is adopted to analyze the velocity of plasma bubbles due to its better performance than histogram of oriented gradient. All-sky images from Hainan Fuke, an example on 17 September 2014, are analyzed to investigate the plasma bubble drift velocities using CMW. For comparison and validation, EPBs motions obtained from three traditional methods are also investigated. The advantages and disadvantages of using CMW are discussed. The results of CMW are compared with slant total electron contents data and show a good consistency, but some errors are also discussed.

**Plain Language Summary** The advantages of our method are as follows. First, CMW can obtain the velocity of different parts in EPB. Second, the result of CMW has a relatively good stability. The disadvantage of CMW is that the computational complexity is sometimes large, because self-adaptive method is used and this process involves looping operations. The result of CMW shows a good consistency with GPS STEC data, which means that the results of CMW are generally reliable.

## 1. Introduction

Equatorial plasma bubbles (EPBs), which are usually observed at equatorial and low-latitude regions, are a kind of special area in the ionosphere where the electron density is relatively lower than the surrounding area. Since the EPBs at low-latitude region usually cause the satellite signal scintillation, it is valuable to investigate the velocity analysis of EPBs at low latitude so as to predict the satellite signal scintillation.

The generation mechanism of EPB was proposed by Dungey (1956), and he thought that the Rayleigh-Taylor instability is the physical mechanism responsible for the generation of EPB. Today this theory is recognized commonly.

In the last several decades, a variety of instruments were used to observe the EPBs. In general there are two methods. One is the radio method such as global ground-based Global Positioning System (GPS) receiver networks, very high frequency scintillation measurements, ionogram, and so on (Ning et al., 2012; Nishioka et al., 2008; Weber et al., 1982). According to the radio method like using ionosonde, Equatorial Spread-F is a phenomenon in the ionogram that produces large turbulent variations of electron density at *F* region. This phenomenon is usually related to EPBs (Fejer et al., 1999; Sultan, 1996).

Because of the photochemical reaction mechanism, airglow can indirectly reflect the electron density. As the result airglow methods can also be used to observe EPBs. Initially, photometer and Fabry-Perot

interferometer helped us to understand the ionosphere by observing airglow. These instruments are good at observing single point information but are not conducive to observing two-dimensional information. As instruments improved, researchers begin to apply two-dimensional imaging technique to study phenomena in the ionosphere, including EPBs. The early report on all-sky airglow observations of EPBs were reported by Weber et al. (1978). They obtained equatorial and near-equatorial 630-nm airglow observations by using all-sky imager. The north-south aligned airglow depletion regions were found in the images. These depletion regions often extend more than 1,200 km in the north-south direction and 50–200 km in the east-west direction. They drift toward east in most of the cases, but in one case they drift toward west after local midnight. Later, another evolution of imaging technique occurred when the charge-coupled device was utilized. This technique improved the temporal resolution and promoted the study of dynamics of the ionosphere (Makela, 2006). In the last 20 years, many studies of EPBs using airglow observations were published (Makela, 2006; Mukherjee et al., 1998; Ogawa et al., 2005; Sahai et al., 1994). The spatial distribution of EPB is an electron depletion tube extended across the magnetic equator along the magnetic field lines. This was verified by Martinis and Mendillo (2007) and Hyosub et al. (2009). There are many other aspects about EPBs that were studied mainly by using airglow observations, such as seasonal variations of EPBs occurrence (Sekar et al., 2004), zonal drift velocity (Abdu et al., 2003; Huang et al., 2010), the westward tilts with increasing poleward latitude (Abalde et al., 2001; Mendillo & Baumgardner, 1982), bifurcations and secondary structure (Mendillo & Baumgardner, 1982; Pimenta, Fagundes, Bittencourt, & Sahai, 2001), seasonal and solar cycle effects (Sahai et al., 2000; Tsunoda, 1985).

The EPB drifts eastward in most cases. It is affected by *F* region dynamo electric field, which is associated with zonal neutral winds. This *F* region dynamo electric field was explained by Hyosub et al. (2009). Some details of electric field inside and outside the EPBs were discussed by Huang et al. (2010). But sometimes, the EPB eastward velocity may turn into steadily increasing westward velocity that lasted till early morning hours because of the disturbance dynamo effect (Abdu et al., 2003). In general, there are three different methods to calculate the drift velocity of EPBs currently using airglow observations. The first one was used by Pimenta, Fagundes, Bittencourt, Sahai, Gobbi, et al. (2001). Because the EPB in the airglow images is a dark band extending in the north-south direction and the gray value of pixels in dark band are lower than other brighter surrounding area, so he extracted all the pixels at the same latitude line which is across the EPB and got a curve of the pixel gray value; the depression in this curve represents the EPB region. Then he used the movement of the depression's west wall to calculate the drift velocity, because it is more stable than using the east wall due to the expansion movement of EPB. Paulino et al. (2011) used this method to study the EPB drift velocity in Brazilian. The second method was used by Sharma et al. (2012). He used the movement of the EPB west boundary in the airglow images to calculate the drift velocity. The reason why he did not use the east boundary is also related to the stability. The third method, which is used by Liu (2015), is called keogram. The first step is to extract the same narrow latitude regions across the EPB areas in a series of successive airglow images. The second step is to stack all the narrow latitude regions in chronological order and there will be a dark stripe tilted to the drift direction. The slope of the dark stripe is the average drift velocity of EPB.

All these three methods still have some disadvantages. In the first and second methods the expansion movement of EPBs is not calculated. Because the east wall or east boundary is not used. The third method only can obtain the average velocity value. So in this paper a new method to calculate the EPB drift velocity was put forward. It is called cloud motion wind (CMW), which is widely used in meteorology. This technology is used to calculate the drift velocity of different pieces of clouds and estimate the wind field (Li et al., 2009; Liu & Liu, 2003; Yang et al., 2013; Zhao et al., 2012). Using this technology, EPB will be split into many small pieces or windows and every window has one drift velocity so that many details of drift can be manifested. Two suitable images are enough to calculate one case of EPB drift. If there is a series of successive airglow images, not only the average velocity but also the velocity at different moment can be obtained.

## 2. Instrument and Observation

The observations adopted in this paper come from the all-sky imager in Hainan Fuke station (19.5°N, 109.2°E) supported by China Meridian Project. This station is located at low-latitude area and can observe EPBs easily for the reason that EPBs usually appear at equatorial and low-latitude area. The all-sky imager uses a fish-eye

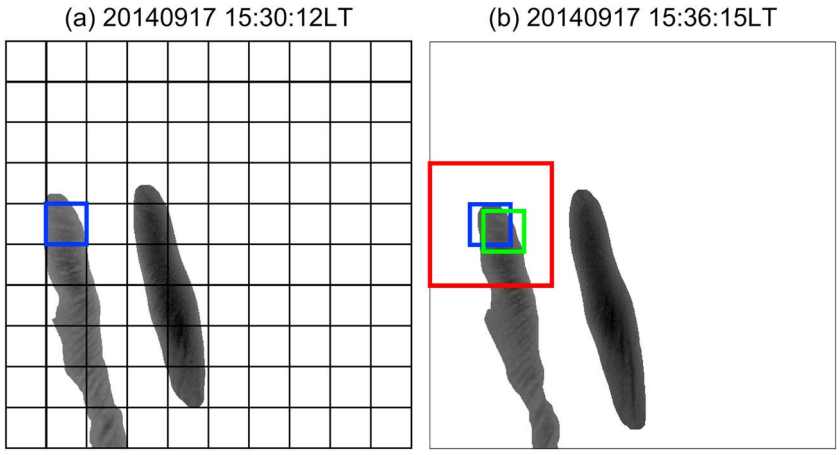


**Figure 1.** Example of the cloud motion wind arithmetic using the pretreated airglow images obtained at 15:30:12 LT and 15:36:15 LT on 17 September 2014. The black rectangles are tracing windows. The blue rectangle in (a) is the tracing window being processed. The blue rectangle in (b) indicates the same position as in (a). The red rectangle is the searching area, and the green rectangle is the target window which matches the blue tracing window in (a).

lens with 180° viewing angle. It can get the information of airglow from a hemispherical area. The diameter of this area is approximately 1,400 km at 300-km altitude. The imager can map this hemispherical area to a circular image. A 630.0-nm interference filter is installed at the all-sky imager. We assumed that 630.0-nm airglow emission comes from 300 km. By doing so, the images used in this study show the information of ionosphere at about 300 km.

The observation is a circular image whose diameter is 1,024 pixels. Since the fish-eye lens causes large deformation at the edges of the image, the smaller circular area with 903 pixels as the diameter was used and the rest was deleted. This smaller circular area corresponds to the zenith angle ranging from 0° to 84°. Before calculating the velocity of EPBs, images were treated by a pretreatment process, which includes image extraction, image enhancement, orientation correction, and image projection. After pretreatment, EPBs in the images were shown clearly and velocity analysis could be more accessible because every pixel in the image was projected to the corresponding latitude and longitude, so the distance between two pixels could be easily obtained.

## 3. Methodology

The main problem discussed in this study is how to calculate the velocity of different parts of EPBs. The technology applied here is CMW method. It is a way to show the velocity of different parts of clouds then to speculate the velocity vector field of wind under the premise that the clouds are driven by wind. Because the main problem here is how to get the velocity vector field of EPB, so the power which causes the EPB drift is not investigated in this paper.

Before applying CMW to calculate the drift velocity of EPBs, two things have to be done. One was to pretreat the images and choose two pretreated images that can clearly observe the EPBs. The pretreatment process is discussed in section 3.1. The two images were obtained on the same day and there were a few minutes difference between the two images' obtaining times. Another thing was to extract EPBs area from the background, which is discussed in section 3.2.

There were four steps to use CMW to calculate the velocity vector field of EPB drifts which is shown in Figure 1 The two images were obtained at 15:30:12 LT and 15:36:15 LT on 17 September 2014, respectively. The first step was to separate the image (a) into many square tracing windows (black rectangle) of the same size and check each window successively. If the current window has the EPB information, proceed to the next step. If not, check the next window. One of the windows which have the EPB information is shown as a blue rectangle in image (a). Second step was to expand a square searching area in image (b), which is shown as a red rectangle. This searching area regards the position of the blue tracing window in image (a) as the center.

The position of the blue rectangle in image (b) is the same as that in image (a). The third step was to find a target window (green rectangle) with the same size as the blue tracing window from all the windows in the searching area. This target window was the most similar to the blue tracing window. In other words, this green rectangle was seen as the window displaced from the blue tracing window. The fourth step was to calculate the velocity of the blue tracing window by using the displacement between the blue tracing window and the green target window. Then the same steps are repeated until each tracing window that had the EPB information in image (a) had a drift velocity.

The most important part in the process of CMW is how to find the target window as accurately as possible. The most commonly used method is the maximum correlation coefficient method (MCC; Yang et al., 2013). This method uses the correlation coefficient of two-dimensional matrixes to determine the similarity between tracing window and target window. We adopted MCC to do the CMW process. Another method called *histogram of oriented gradient* (HOG; Jamshed et al., 2015) was adopted too, which uses the HOG of the gray value as a feature to identify the motion of objects in images. HOG is usually adopted to identify the motion of people in pictures, but here it is used to identify the motion of EPBs.

### 3.1. Pretreatment Process

The data obtained directly from the all-sky airglow imager at Fuke station in Hainan are photographs taken every 3 min. The photos are grayscale images. The grayscale value ranges from 0 to 255. But when the images were under the pretreatment, this range was converted to 0–1. There are some defects of the image that prevented the subsequent extraction of EPB information. So the pretreatment process is necessary. During the pretreatment process the presumed altitude of the airglow information was 300 km. Before introducing the pretreatment process, there is a software called *Stellarium* that needed to be introduced. Stellarium is a kind of planetarium software that shows exactly what you see when you look up at the stars. When you set the observation location and time, it can provide the zenith and azimuth of each star. This software was used during the pretreatment process. The defects and corresponding preprocessing steps are as follows. The pretreatment process is also shown in Figure 2. The case used here was obtained at 00:20:45 LT on 27 September 2014. Figure 1a is the original image.

#### 3.1.1. Image Extraction

Since the imager uses a fish-eye camera, the edge information of the grayscale image is severely deformed and the information in the central circular area is valid. So the valid area needs to be extracted and the deformed area needs to be removed. The extracted image is shown in Figure 2b. The process of image extraction is as follows:

1. Three evenly distributed stars were found in clear image and the Stellarium software was used to obtain the azimuth of the three stars. Then we put it into the cosine formula, as shown in equations (1)–(3), to calculate the zenith coordinate of the instrument's location in Figure 2a.

$$\frac{(X_2-X_0)\cdot(X_1-X_0)+(Y_2-Y_0)\cdot(Y_1-Y_0)}{\sqrt{(X_2-X_0)^2+(Y_2-Y_0)^2}\cdot\sqrt{(X_1-X_0)^2+(Y_1-Y_0)^2}}=\cos\theta_1 \tag{1}$$

$$\frac{(X_3-X_0)\cdot(X_1-X_0)+(Y_3-Y_0)\cdot(Y_3-Y_0)}{\sqrt{(X_3-X_0)^2+(Y_3-Y_0)^2}\cdot\sqrt{(X_1-X_0)^2+(Y_1-Y_0)^2}}=\cos\theta_2 \tag{2}$$

$$\theta_1=Azim_2-Azim_1,\quad \theta_2=Azim_3-Azim_1 \tag{3}$$

Here $(X_0, Y_0)$ is the required zenith coordinate. The positions of the three stars in the image are $(X_1, Y_1)$, $(X_2, Y_2)$, and $(X_3, Y_3)$. The corresponding azimuth angles are $Azim_1$. $Azim_2$, and $Azim_3$

2. A circular area with a radius of 451 pixels and with a center on the zenith coordinate was extracted. Meanwhile, the edge information was removed. The result is shown in Figure 2b.

#### 3.1.2. Image Enhancement

The gray value of the original image directly obtained from the instrument is generally low, so the low brightness makes the information in the image unclear. The process of image enhancement was used. The enhanced image is shown in Figure 2c and the steps are as follows:

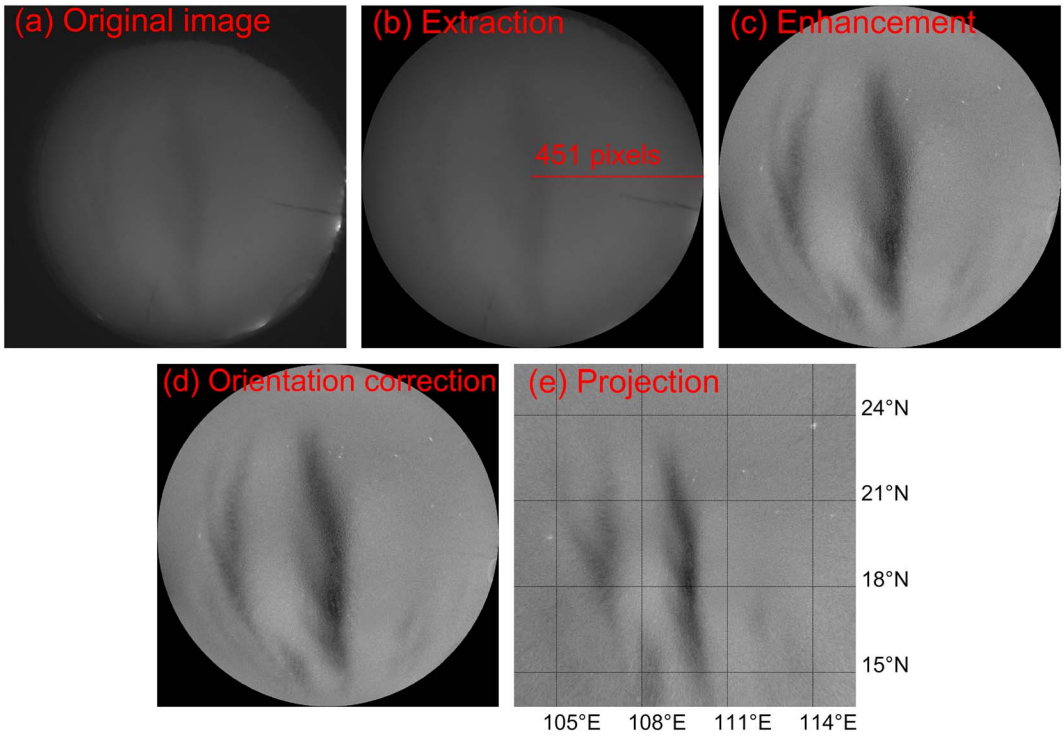


**Figure 2.** Example of the pretreatment process using the airglow image obtained at 00:20:45 LT on 27 September 2014. (a) The original image. (b) The extracted image; the red line indicates the radius of the extracted area which is 451 pixels. (c) The enhanced image. (d) The orientation corrected image. (e) The projected image.

1. The average grayscale value $\overline{P}$ of the valid circular area in Figure 2b was calculated. Then the image's grayscale value range was stretched from 0–2×$\overline{P}$ to 0–1 by using the *imadjust* function in Matlab. This function can map the values in Figure 2b to new values in Figure 2c such that values between 0 and 2×$\overline{P}$ map to values between 0 and 1. The values above the 2×$\overline{P}$ map to 1.
2. In order to make the EPB information obvious, the effect of background radiation needed to be removed. In this paper, the average image of 20 consecutive images was used as the background information of them. Then the background information was subtracted from these 20 images to achieve the purpose of removing background radiation. After this, the image's grayscale value range was stretched again from minimum–maxmum to 0–1.

### 3.1.3. Orientation Correction

Another defect is that the orientation of the image needs to be adjusted due to the placement of the instrument. The orientation of the image should be adjusted to be north in up direction and east in right direction. The orientation-corrected image is shown in Figure 2d. The process of orientation correction is as follows:

The method of correction in this paper was to find the position of Polaris in the image and bring its position coordinates and zenith position coordinates into formula (4). Thereby, the angle that needed to be rotated was calculated. In addition, the Polaris itself has a small azimuth that can be obtained from the Stellarium software. This small angle should be considered when calculating the rotation angle. Finally, the image was rotated according to the obtained angle.

$$\theta = -\arctan\frac{X_0 - X_p}{Y_0 - Y_p} - \alpha \tag{4}$$

In this formula, ($X_0$, $Y_0$) is the zenith position coordinates and ($X_p$, $Y_p$) is the position coordinates of Polaris. The variable $\alpha$ is the azimuth angle of Polaris; $\theta$ is the rotation angle which needs to be calculated.

#### 3.1.4. Image Projection

The image captured by the fish-eye camera is distorted and cannot be consistent with the latitude and longitude of the ground. So the image needs to be projected to the latitude and longitude. The projected image is shown in Figure 2e and the process of image projection is as follows:

1. Forty stars were found in clear image, and their position coordinates, elevation, and azimuth were recorded.
2. The distances from the 40 stars to the center of the image were calculated. These distances were fitted with the corresponding zenith angle (the complement angle of the elevation angle) of each star to obtain the relationship between distances and angles.
3. The location of the station is 19.5°N, 109.2°E. The largest zenith angle of the circular area extracted during image extraction process is 84°. So according to geometric relations, the projection range of the image should be 13.5°–25.48°N, 103.22°–115.2°E.
4. According to the projection range, a latitude and longitude grid was created. Grid point spacing was 0.02°. Then each grid point had a set of zenith and azimuth angles at the altitude of 300 km basing on geometric relationships. Thus, the fitting relationship between the zenith angle and the distance obtained in the second step could be used to calculate the distance between the grid point and the center. Finally, according to the azimuth angle, each grid point could have a corresponding coordinate in the circular area. This was the projection relationship between the grid and the circular area.
5. According to the projection relationship, the pixel values in the circle range were assigned to the latitude and longitude grid points (If the coordinates were not integers, then take the nearest). Then a projected image was obtained as shown in Figure 2e.

### 3.2. Extract Plasma Bubbles Information

In order to reduce the computational complexity, the EPB areas should be extracted from the background and only to consider the information in the EPB areas. Because the EPB areas are nebulous features in the airglow image, the general boundary identification algorithm cannot be applied directly to identify EPB boundary. So in this study, extraction process was divided into three steps. Figure 3 shows this process. The case used here was the airglow image obtained at 22:36:12 LT on 28 September 2014. Figure 3a is the image after pretreatment. Nos. 1 and 2 represent the EPBs that we want to extract.

First step, the images were smoothed by average filter to reduce noise. An average filter in the size of $19 \times 19$ pixels was used to do the smoothing. When the average filter slid through the entire image, the image smooth process was finished. The smoothed image is shown in Figure 3b.

Second step was to distinguish EPBs and background using binarization. It means manually setting a suitable threshold value, and the pixel gray value below the threshold was changed into 1 which means white, and the pixel gray value higher than the threshold was changed into 0 which means black. By doing this, a binary image just like (c) was obtained in which the white pixels represent the EPB areas and the black pixels represent the background. The threshold here was 0.245.

The third step was to extract the EPB information. For the pretreated image as shown in (d), according to the boundary of white area in image (c), the gray values of pixels inside the boundary were maintained and those outside the boundary were changed into white. By doing this, image (e) was obtained, in which the EPB information was extracted and the background was white. Here the extraction process was finished.

### 3.3. MCC Method

MCC method can give a correlation coefficient calculated from two two-dimensional matrices of the same size, and the correlation coefficient, which is a number from $-1$ to 1, describes the correlation of two matrices. The lager the absolute value of the correlation coefficient, the more correlated the two matrices. However, the positive and negative correlation coefficients represent positive correlation and negative correlation, respectively. The tracing window in the earlier image and the target window in the later image were just two two-dimensional matrices of the same size. So this method could find a target window from the searching area that was most similar to the tracing window according to the fact that the correlation coefficient between this most similar target window and the tracing window was the maximum among all the other windows in the searching area. Here the positive correlation coefficient was only considered. This

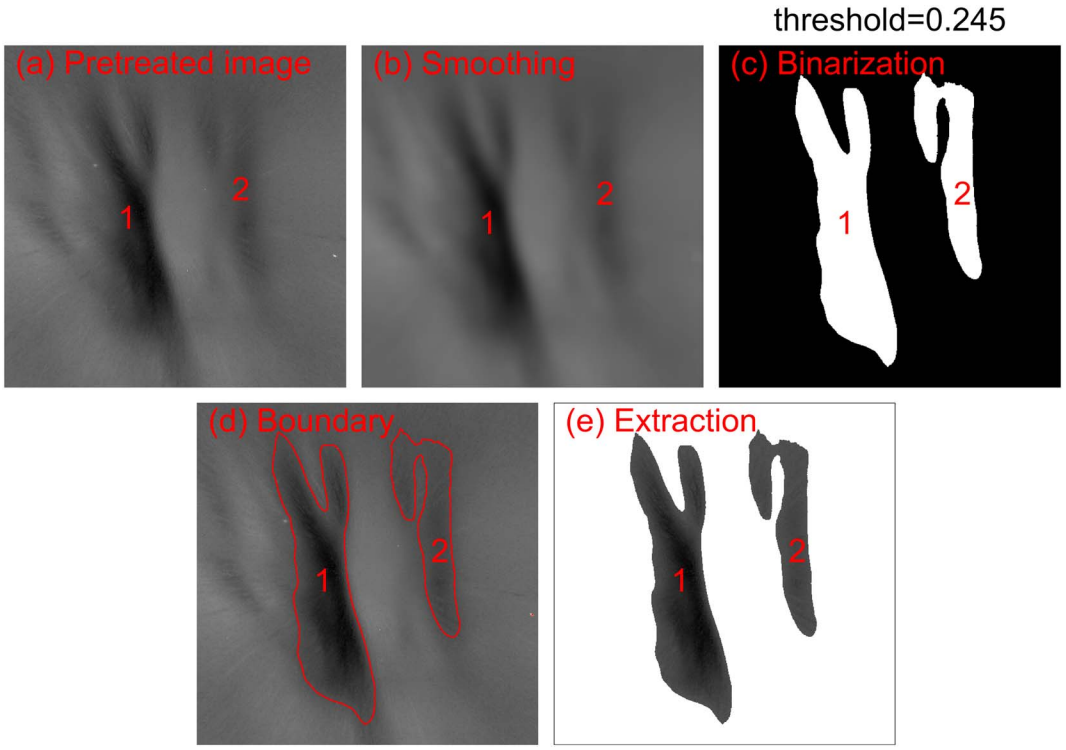


**Figure 3.** Example of the equatorial plasma bubble (EPB) extraction process using the airglow image obtained at 22:36:12 LT on 28 September 2014. (a) The pretreated image; nos. 1 and 2 represent the EPBs we want to extract. (b) The smoothed image. (c) Binary image using the threshold of 0.245. (d) The boundary of EPBs. (e) The EPB extracted image.

method refers to the cross-correlation method put forward by John A. Leese et al. (1971). The formula (5) shows how to calculate the correlation coefficient.

$$R(m,\ n)=\frac{\sum\limits_{i}\sum\limits_{j}\left(f(i,\ j)-\overline{f}\right)\left(g(i+m,\ j+n)-\overline{g}\right)}{\left\{\sum\limits_{i}\sum\limits_{j}\left[f(i,\ j)-\overline{f}\right]^{2}\sum\limits_{i}\sum\limits_{j}\left[g(i+m,\ j+n)-\overline{g}\right]^{2}\right\}^{1/2}} \tag{5}$$

According to formula (5), $i, j$ refer to the pixel's row and column numbers in the image; $m, n$ refer to the differences of row and column numbers between the positions of target window and tracing window; $f(i,j)$ and $g(i+m,j+n)$ refer to the gray value of the pixel in tracing window and target window, respectively, the gray value ranges from 0 to 1, and the average gray value for all pixels in the tracing window and target window are $\overline{f}$ and $\overline{g}$; $R(m,n)$ refers to the correlation coefficient between the tracing window and the target window.

Every target window in the searching area could calculate a correlation coefficient with the tracing window. The target window with the MCC was the most similar one. So drift velocity of the tracing window can be obtained according to the displacement between the most similar target window and the tracing window.

### 3.4. HOG

HOG is a method using the histogram of oriented gradient to describe the feature of a two-dimensional matrix. This method is adopted for human detection (Jamshed et al., 2015). We treated the HOG as a feature vector and then calculated the Euclidean distance of the two feature vectors of tracing window and target window. The shorter the distance, the more similar the two windows are. So in this study, HOG was used to find the most similar target window in the searching area.

Before calculating the HOG, the gradient of every pixel in the image should be known. The formulas (6)–(8) show how to calculate the gradient.

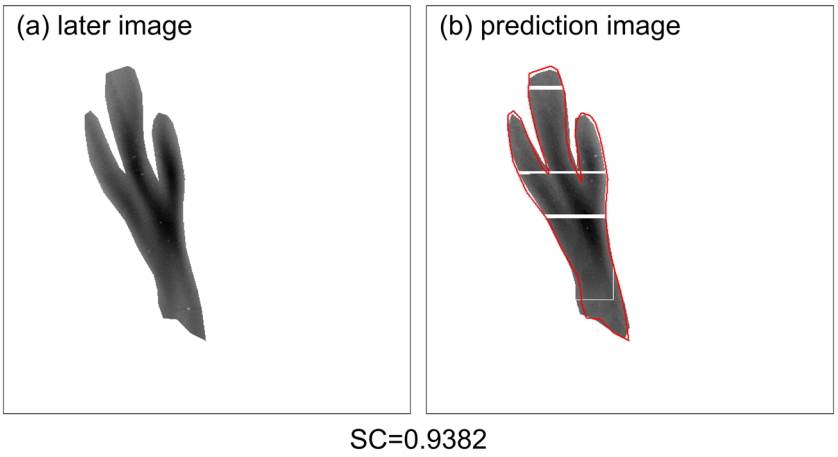


**Figure 4.** Example of calculating the similarity coefficient (SC) using the airglow images obtained at 21:50:09 LT and 21:59:14 on 25 October 2013. (a) The equatorial plasma bubble area extracted from the later image; (b) the image formed by moving tracing windows in the earlier image according to the result of cloud motion wind; the red line is the boundary of equatorial plasma bubble area in (a).

$$G_x(i,j) = f(i,j+1) - f(i,j-1) \tag{6}$$

$$G_y(i,j) = f(i+1,j) - f(i-1,j) \tag{7}$$

$$G(i,j) = \sqrt{G_x(i,j)^2 + G_y(i,j)^2} \tag{8}$$

$G_x(i,j)$ refers to the zonal gradient of the pixel in the $i$ row and $j$ column, the east direction is positive; $G_y(i,j)$ refers to the meridional gradient of the pixel in the $i$ row and $j$ column, the north direction is positive; $G(i,j)$ refers to the gradient value of the pixel in the $i$ row and $j$ column; $f$ is the gray value of the pixel in the specified row and column.

A gradient field was obtained after calculating the gradient of each pixel in the image. The pixels on the edge of image could not calculate the gradient using formulas (6)–(8), so they were abandoned. Both the earlier image and the later image could generate a gradient field, respectively, so there were an earlier gradient field and a later gradient field. Then the main idea of HOG is just like MCC discussed above, except that we use the gradient fields and Euclidean distance instead of EPBs extracted images and correlation coefficient. The way to obtain the HOG can be found in the literature written by Jamshed et al. (2015).

### 3.5. Other Processing

The main calculation methods were described above, but there were also some problems needed to be solved. The first problem was how to evaluate the result of CMW. The solution is shown in Figure 4. The data used in this case were two airglow images obtained at 21:50:09 LT and 21:59:14 on 25 October 2013. The later image is shown in image (a). The tracing windows in the earlier image were moved according to the result of CMW and then a prediction image was generated as shown in image (b). In order to clarify the discrepancy between images (a) and (b), the boundary of EPB in image (a) is also plot on image (b) using red line. We can see some mismatches on the boundary and some cracks inside the EPB area in image (b). The details are discussed in section 4.4. Then we calculate the correlation coefficient between the later image and the prediction image to evaluate their similarity. To distinguish between this correlation coefficient of two images and the correlation coefficient of two windows discussed in section 3.3, the correlation coefficient here are called similarity coefficient (SC) in the following discussion. The SC in this case shown in the figure was 0.9382. The higher the SC, the better the CMW result is.

The second problem was how to choose suitable sizes of tracing windows and searching areas. The self-adaptive method was used to solve this problem. In this method the tracing window sizes changed from $40 \times 40$ to $60 \times 60$ pixels and the step was 4 pixels. The searching area sizes changed from $3 \times 3$ to $5 \times 5$ windows and the step was one window. These two change ranges were determined by experiments of 10 cases

including large-scale EPBs and small-scale EPBs. For each case a two-dimensional matrix could be obtained, one dimension was tracing window sizes, another was searching area sizes. The elements of the two-dimensional matrix were SCs of CMW results by using corresponding combinations of the two sizes. If the maximum of the SCs was at the edge of the two-dimensional matrix, then the ranges of these two dimensions would be adjusted to let the maximum of SCs locate inside the matrix (not the edge of the matrix). According to these experiments the two change ranges of self-adaptive method were determined. This self-adaptive method was used in CMW process to choose suitable sizes of tracing windows and searching areas basing on the assumption that the combination of two sizes with the maximum SC is the best choice.

The third problem was that all the EPBs in this study drifted eastward; however, the searching area covered all areas around the tracing window and this resulted in a lot of unnecessary calculations. So that the west half searching area was not considered in the calculation in order to reduce the computational complexity. Although the EPB drift direction may change into westward due to the disturbance dynamo during magnetic storm time (Blanc & Richmond, 1980), in this study we did not find such a situation. If the EPBs did not drift or dilate westward, this solution might cause problems. But first, we did not see any dead EPBs. Second, the time interval between two successive images was long enough so that the westward dilation did not affect the eastward drift. Because drift produced more significant change than dilation. According to these, only to use the east half searching area was feasible. If there are cases of westward drift or other situation, we can activate the entire searching area.

The fourth problem was that the searching area might be a little small for some tracing windows. Secondary search was used to solve this problem. Secondary search means that if the best target window was at the edge of the searching area, a secondary searching area, which regarded this best target window as center, was set to find a maybe better target window in this secondary searching area.

The fifth problem was that when using the MCC, though the best target window was found according to the correlation coefficient between the tracing window and the target window, even the largest correlation coefficient might not be large enough. So in this study a standard value of 0.5 was set to determine whether the correlation coefficient was qualified. The qualified correlation coefficient was larger than 0.5 and the unqualified correlation coefficient was less than 0.5. If the correlation coefficient between the best target window and the tracing window was unqualified, this velocity of the tracing window would be deleted and interpolation is used instead. The interpolation was calculated using the velocities with qualified correlation coefficient around the position where unqualified velocity was located. Formula (9) shows how to calculate the interpolation.

$$P = \frac{\sum_{k=1}^{N} P_k I_k}{\sum_{i=1}^{N} I_i} \tag{9}$$

In this formula, $P$ refers to the zonal component of the interpolation velocity vector. $N$ refers to the number of all the qualified velocity vectors involved in the calculation. $P_k$ refers to the zonal component of the $k$th qualified velocity vector of all the qualified velocity vectors. $I_k$ refers to the distance between the position where the $k$th qualified velocity is located in and the position where the unqualified velocity is located in. $I_i$ refers to the distance between the position where the $i$th qualified velocity is located in and the position where the unqualified velocity is located in. This is also the same formula used to calculate the meridional component of the interpolation vector.

## 4. Results and Discussion

### 4.1. Velocity Vector Field

The result of one case is shown in Figure 5. It is an example during 23:30:12–23:33:14 LT on 17 September 2014 showing the velocity vector field of EPBs. The velocity vector field of EPBs is shown by red arrows. The zonal and meridian components of the velocity vectors are shown by blue arrows. The velocity values of different tracing windows range from 98 m/s to 144 m/s. Zonal components range from 95 m/s to

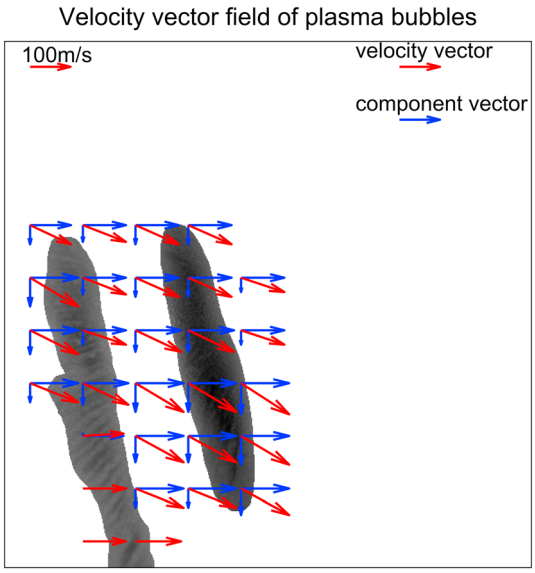


**Figure 5.** An example that shows the result of cloud motion wind using the images at 00:06:34 LT and 00:15:39 LT on 17 September 2014. The red arrows indicate the velocity vector field of equatorial plasma bubble drift. The blue arrows indicate the zonal or meridian components of velocity vectors. The length of arrow representing 100 m/s is shown at the upper left corner of the figure.

124 m/s. Meridian components range from 13 m/s to 77 m/s. According to this, the meridian velocity is relatively smaller than the zonal velocity.

Because the meridian displacements of EPBs are inconspicuous, so there is a little research on the meridional drift velocity of EPBs. One research about it was reported by Mendillo and Baumgardner (1982). They used 630 nm airglow imaging system to study the airglow characteristics of EPBs. The drift velocities were computed by using the assumed altitude of 300 km, which is consistent with the study in this paper here. The EPBs were observed to drift eastward with zonal velocity of 80–190 m/s, and the northward drift of about 50 m/s was obtained from a few cases. This result also shows the fact that the meridian velocity is relatively smaller than the zonal velocity.

The velocity calculated by CMW is consistent with previous conclusions. Both the meridian velocity and the zonal velocity can be computed by using CMW method. This is one of the advantages of CMW.

### 4.2. Discussions About CMW

The relationship between the size of tracing window and the SC is shown in Figure 6. According to Figure 6 there is a trend that as the tracing window size becomes larger the SC becomes larger too. In addition, the SCs are overall larger than 0.7. This indicates that it is feasible to calculate the velocity vector field of EPBs by CMW. The difference between two methods is shown in Figure 6, too. The advantage of MCC over HOG is obvious. Because MCC was better than HOG in most cases, the MCC was used to calculate the velocity vector field of EPBs in later discussion.

Additionally, when using the MCC, there were only a few unqualified correlation coefficients (defined in the discussion about the fifth problem in section 3.5), just only one or two among all the correlation coefficients in one case, so the velocities of the tracing windows were basically calculated by CMW rather than interpolation.

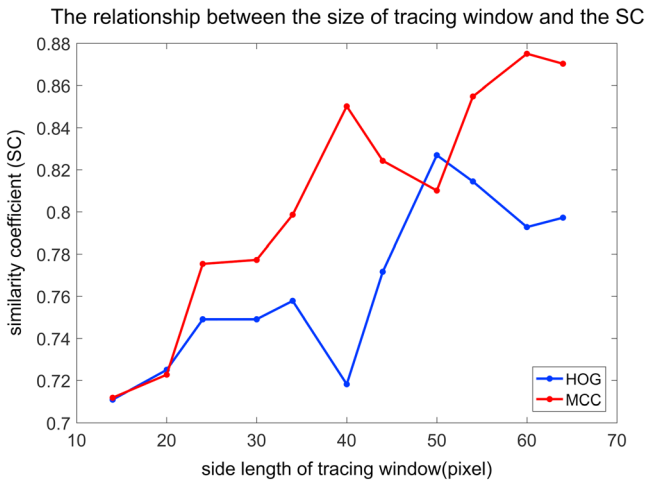


**Figure 6.** The graph showing that the similarity coefficient (SC) varies with the tracing window size using the airglow images at 00:06:34 LT and 00:15:39 LT on 17 September 2014. Red curve shows the result using MCC method; blue curve shows the result using HOG method. MCC = maximum correlation coefficient; HOG = histogram of oriented gradient.

### 4.3. CMW Compared With Traditional Methods

In order to verify the reliability of the results and analyze the advantages and disadvantages of different methods, the results of CMW using MCC were compared with the results of three kinds of traditional methods using 32 successive images during 23:18:05 LT to 00:52:02 LT on 17 September 2014. The zonal velocity at latitude of 17.7°N was calculated by using these different methods. Traditional method 1 refers to the method used by Pimenta, Fagundes, Bittencourt, Sahai, Gobbi, et al. (2001). Traditional method 2 refers to the method used by Sharma et al. (2012). Traditional method 3, which is called keogram, refers to the method used by Liu (2015). Figure 7 shows the keogram image of 32 successive images we used. The red points are the central location of EPBs and the red lines are one-dimensional polynomial fitting-curves of red points. The slopes of the red lines are the zonal drift velocity of EPBs.

Figure 8 shows the zonal drift velocity calculated by CMW and three traditional methods at different local time from 23:18:05 LT to 00:52:02 LT on 17 September 2014. Figure 9 shows the average velocity and the variance of these four different calculation methods. According to Figure 9, the average values of zonal velocity calculated by the four methods are basically the same. But the variances differ greatly. Method 1 has the largest variance, which means it calculated the most unstable zonal velocity. Method 2 has the second larger variance and CMW has the third. The variance of keogram is zero, which means it calculated the most stable

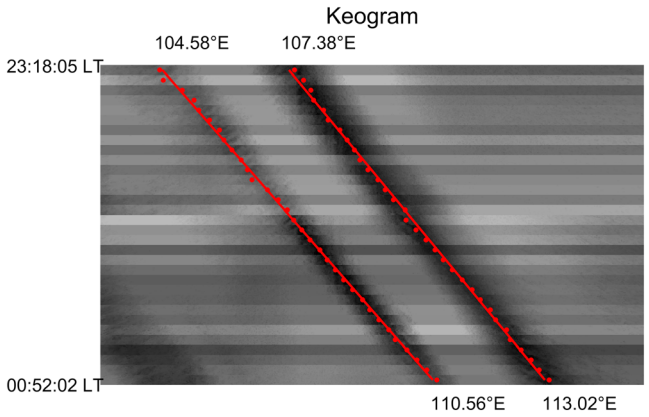


**Figure 7.** Example of using keogram to calculate the zonal velocity of equatorial plasma bubbles drift. Images during 23:18:05 LT to 00:52:02 LT on 17 September 2014 were used. The red points are the central locations of equatorial plasma bubbles at each moment and the red lines are one-dimensional polynomial fitting curves of red points.

zonal velocity but the value has no variation. The stability difference is also shown in Figure 8, the curves of methods 1 and 2 have relatively large variation range. The curve of method 1 has the largest variation range even jumps from 270 m/s (eastward) to −50 m/s (westward). Though Pimenta, Fagundes, Bittencourt, Sahai, Gobbi, et al. (2001) and Sharma et al. (2012) both presented that the west wall is more stable than the east wall, the west wall may be unstable too. The curve of keogram only has one value during the period we are concerned with; it is because we adopted one-dimensional polynomial fitting. So the slope of the fitted curve was a fixed value and the velocity unchanged. CMW's results have a relatively good stability and credible average speed value.

The first advantage of CMW is that it can compute both the meridian velocity and the zonal velocity of EPBs at different latitudes and longitudes, but the traditional methods used here cannot do this. The traditional methods can only get the zonal velocity of EPBs at different latitudes. The second advantage of CMW is that when calculating the drift velocity, the effect of EPB deformation is considered. The traditional methods 1 and 2 only use the west wall or west boundary in calculation and the effect of EPB deformation is not considered. So CMW can provide more information than traditional methods 1 and 2.

The disadvantage of CMW is that computational complexity is sometimes large because self-adaptive method was used and this process involves looping operations. In addition the process of extracting EPBs information involves manual intervention. Because the threshold value, which was used to distinguish EPBs and background, was set manually (mentioned in section 3.2), as a result, the velocity value may be influenced by manual intervention.

### 4.4. CMW Compared With STEC Data

To verify the reliability of CMW, we compared the results of CMW with GPS slant total electron content (STEC) data. Thirty-two successive images obtained from 23:18:05 to 00:52:02 LT on 17 September 2014 were used in this verification. Simultaneously, sufficient GPS STEC data were collected by the nearby GPS stations. A lot of stations observed the ionospheric scintillation, which was caused by the EPBs drifting through Hainan region. We selected the data received by four nearby stations from the same satellite. The four stations were hisy (18.24°N, 109.53°E), hihk (19.99°N, 110.25°E), gxwz (23.48°N, 111.23°E), and gdzh (22.28°N, 113.57°E). These data are plotted in Figure 10, which shows the STEC variation with local time. Four STEC time-varying curves with different colors represent four different stations mentioned above. We can see some trough of curves. It was because the total electron density on the GPS signal path decreased. Since the EPB areas are electron density depletion regions, when the GPS signal pass through the EPB areas, this phenomenon may occur. There are also some breakages on STEC curves. It was because the electron density gradient on the GPS signal path was large enough to disturb the signal and make the signal miss. The EPBs also can be the main reason of this phenomenon in the equatorial region. To clarify these phenomena, we fitted four curves and show them by using a red line in Figure 10.

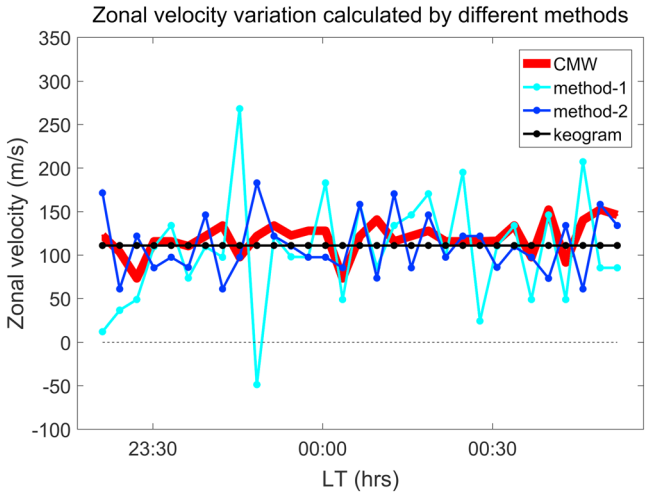


**Figure 8.** The graph showing the zonal drift velocity calculated by CMW and three traditional methods at different local time from 23:18:05 LT to 00:52:02 LT on 17 September 2014. CMW = cloud motion wind.

Fortunately, EPBs as the cause of the ionospheric scintillation were captured by 32 successive images that we selected. So we projected the ionosphere puncture points (IPPs) of the GPS signal received by these four stations in each image. Then we recorded the time when the IPP moved into EPB area and showed these periods by using red shadow regions in Figure 10. Simultaneously we have already had the airglow images formed by moving tracing windows according to the velocity vector field, which was calculated by CMW. IPPs were also

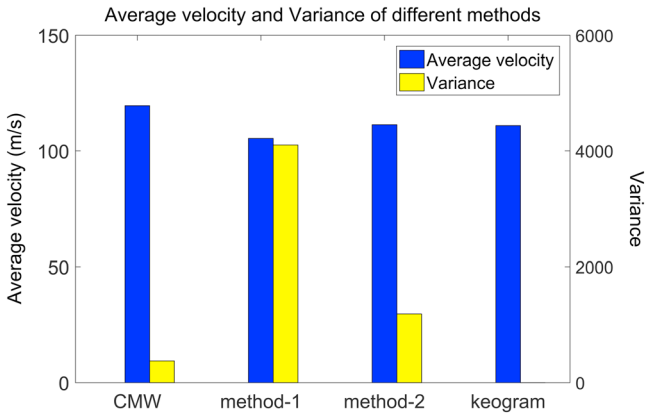


**Figure 9.** The histogram showing the average velocity value and the variance of the data in Figure 8 obtained by CMW and three traditional methods. CMW = cloud motion wind.

projected in these prediction images and the periods when the IPP moved into EPB area in these prediction images are shown by using black shadow regions.

The STEC data show a general consistency with airglow data, but they still have some mismatches and there are also some mismatches between black and red shadow regions, which means CMW still have some error. And so six special moments shown by using a blue dashed curve were selected to discuss the reason. We exhibit six new images calculated by CMW at these six moments in Figure 11, and then we show their IPP points and moving tracks using the color of four stations that coincided with those in Figure 10. The red lines in Figure 11 are the boundary of EPBs in the original images. If IPP is inside the red boundary line, which means this moment belongs to the red shadow region in Figure 10. And if it is inside the black EPB area, this means this moment belongs to the black shadow region. The analysis of mismatches and errors is as follows.

1. In Figure 11, the green IPP at moment (a) and the blue IPP at moment (c) were located around the EPB boundary. According to Figure 10 the green IPP was inside the red boundary line but out of the EPB area formed by CMW and the blue IPP was under the opposite circumstance which means that there were boundary mismatches between original images and new images both at the location of green IPP and blue IPP.
2. The magenta IPP at moment (d) in Figure 10 was inside the red boundary line but out of EPB area, but in Figure 11 we can see that this was not because the boundary mismatch; actually, this was because the magenta IPP was located at a crack in the EPB area formed by CMW in the new image.
3. The magenta IPP at moment (f) and the blue IPP at moment (b) were missing, but they should have escaped the impact of the EPBs and come out. The cyan IPP at moment (e) had entered the EPB area, but the response of STEC was slightly delayed. These phenomena show the mismatch between STEC data and the airglow data. This is probably because the peak height assumed for 630 nm airglow is inaccurate resulting in inaccurate projection of EPBs area on map.

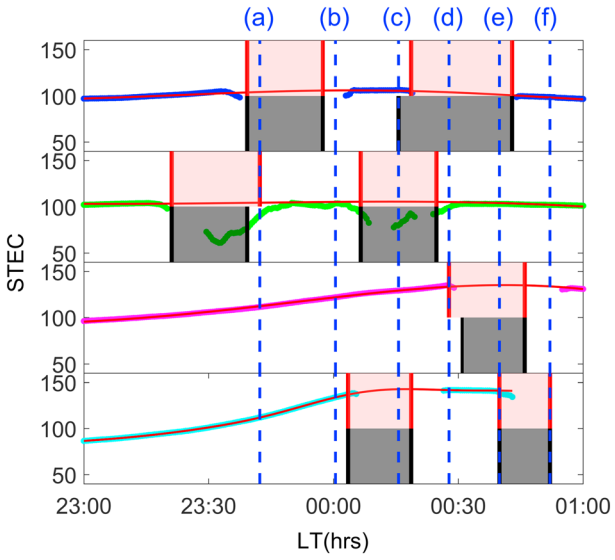


**Figure 10.** Four STEC data curves obtained by four different GPS stations from one satellite during 23:00 LT to 01:00 LT on 17 September 2014. The red curves are the fitted curves of STEC data. The red shadow regions represent the periods that the IPP moved into the EPB region in original airglow images. The black shadow regions represent the periods that the IPP moved into the EPB region in predictive images formed by CMW. The blue dashed represent the spatial moments shown in Figure 11. STEC = slant total electron contents; GPS = Global Positioning System; IPP = ionosphere puncture point; EPB = equatorial plasma bubble; CMW = cloud motion wind.

So there are three kinds of errors, two of them are CMW errors and one is image projection error. The first CMW error is the boundary mismatch which is because the shape of EPBs was changing when they drift, so according to CMW the tracing windows in previous image could not be spliced into the same shape of EPBs in the next image. Another CMW error is that EPB areas formed by CMW have cracks. This is because the size of EPBs was also changing when they drift, so when two adjacent tracing windows are moved according to CMW, they may overlap or separate. When they are separated a crack will appear. The error about the cracks actually proves that the CMW calculated the deformation of EPBs. This is one of the advantages of CMW over other three traditional methods mentioned in section 4.3. And our follow-up work may study how to make up for this error. The reason of image projection error is that the peak height of 630-nm airglow was assumed rather than real one. Actually, 630-nm airglow peak height has a variation range, which is 250–300 km. And we assumed 300 km for image projection. This approximation will result in image projection error.

Though there are some errors of CMW, the consistency between the EPB area formed by CMW and red boundary line is obvious in Figure 11 and the consistency between the black shadow regions and the STEC trough or breakage periods is obvious too in Figure 10. So the results of CMW are generally reliable.

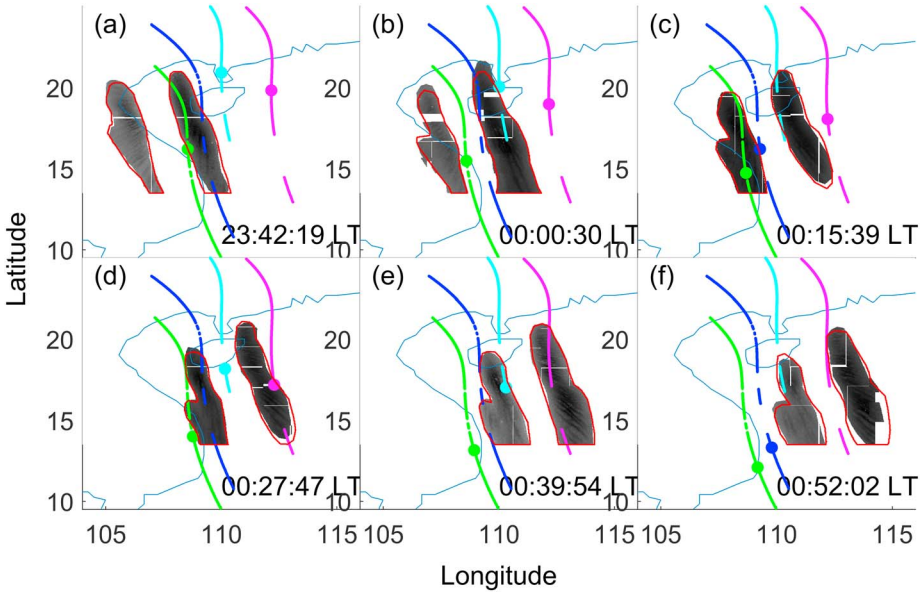


**Figure 11.** Six predictive images formed by cloud motion wind at six spatial moments. The ionosphere puncture points and moving tracks of them are shown by using the color that coincided with the four slant total electron content curves in Figure 10. The red lines are the boundary of equatorial plasma bubbles in original airglow images.

## 5. Summary

The observations of the 630.0-nm airglow emission from the all-sky camera in Hainan Fuke (19.5°N,109.2°E) was used to study the drift velocity of the EPBs. Before calculating the drift velocity, image pretreatment including image extraction, image enhancement, orientation correction, and image projection, was done to make the images clear. After the pretreatment, the EPB areas were extracted from the background using binarization method. Then the velocity vector field of EPBs was calculated using the technology called CMW. There were two matching methods adopted in this technology. One is called MCC; the other one is called HOG. The calculation results of these two methods were compared and it was found that MCC was better than HOG in most cases. So during the velocity analysis in this study, the velocity results were computed by MCC. All the conclusions of this study are as follows.

The velocity vector field of the case during 23:30:12–23:33:14 LT on 17 September 2014 shows that the velocity vector direction is generally from west to east; there are tiny north-south component. The velocity values range from 98 m/s to 144 m/s. Zonal components range from 95 m/s to 124 m/s. Meridian components range from 13 m/s to 77 m/s. It is consistent with previous researches.

The SC between the later image and the prediction image increases as the size of tracing window becomes larger. The SCs are overall larger than 0.7, so it indicates that it is feasible to calculate the drift velocity of EPBs using the technology of CMW. The comparison between MCC and HOG is investigated and MCC is better than HOG in most cases.

By contrast with the traditional methods, using CMW with MCC has some advantages and disadvantages. The advantages are as follows. First, CMW can obtain the velocity of different parts in EPB. This means it can compute both the meridian velocity and the zonal velocity of EPBs at different latitudes and longitudes. This is the advantage over all the traditional methods. Second, during the process of CMW the effect of EPB deformation is considered but traditional methods 1 and 2 are not. Finally, the result of CMW has a relatively good stability. The disadvantage of CMW is that the computational complexity is sometimes large because self-adaptive method was used. In addition the process of extracting EPBs information has great influence on the result of CMW. So in a sense, CMW is susceptible to other process related to it.

To verify the reliability of CMW, we compared the results of CMW with GPS STEC data. The result of CMW shows a good consistency with GPS STEC data which means that the results of CMW are generally reliable. But CMW still has some errors. It is because the size and shape of EPB areas changed when they were

drifting. And the peak height assumed for 630-nm airglow plays an important role in calculating the drift velocity of EPBs, but there is not much research on how to assume airglow peak height.

**Acknowledgments**
This work was supported by the Strategic Priority Research Program of Chinese Academy of Sciences (grant XDA17010207) and the National Natural Science Foundation of China (grants 41574147, 41231065 and 4154145). The authors thank the China Meridian Project for kindly providing the airglow data (http://data.meridianproject.ac.cn).

## References

Abalde, J. R., Fagundes, P. R., Bittencourt, J. A., & Sahai, Y. (2001). Observations of equatorial *F* region plasma bubbles using simultaneous OI 777.4 nm and OI 630.0 nm imaging: New results. *Journal of Geophysical Research*, *106*(A12), 30331–30336. https://doi.org/10.1029/2001JA001115

Abdu, M. A., Batista, I. S., Takahashi, H., Macdougall, J., Sobral, J. H., Medeiros, A. F., et al. (2003). Magnetospheric disturbance induced equatorial plasma bubble development and dynamics: A case study in Brazilian sector. *Journal of Geophysical Research*, *108*(A12), 1449. https://doi.org/10.1029/2002JA009721

Blanc, M., & Richmond, A. D. (1980). The ionospheric disturbance dynamo. *Journal of Geophysical Research*, *85*(A4), 1669–1686. https://doi.org/10.1029/JA085iA04p01669

Dungey, J. W. (1956). Convective diffusion in the equatorial *F* region. *Journal of Atmospheric and Terrestrial Physics*, *9*(5–6), 304–310. https://doi.org/10.1016/0021-9169(56)90148-9

Fejer, B. G., Scherliess, L., & Paula, E. R. D. (1999). Effects of the vertical plasma drift velocity on the generation and evolution of equatorial spread-*F*. *Journal of Geophysical Research*, *104*(A9), 19859–19869. https://doi.org/10.1029/1999JA900271

Huang, C. S., Beaujardiere, O. D. L., Pfaff, R. F., Retterer, J. M., Roddy, P. A., Hunton, D. E., et al. (2010). Zonal drift of plasma particles inside equatorial plasma bubbles and its relation to the zonal drift of the bubble structure. *Journal of Geophysical Research*, *115*, A07316. https://doi.org/10.1029/2010JA015324

Hyosub, K., Heelis, R. A., Paxton, L. J., & Seung-Jun, O. (2009). Formation of a plasma depletion shell in the equatorial ionosphere. *Journal of Geophysical Research*, *114*, A11302. https://doi.org/10.1029/2009JA014369

Jamshed, M., Parvin, S., & Akter, S. (2015). Significant hog-histogram of oriented gradient feature selection for human detection. *International Journal of Computer Applications*, *132*(17), 20–24. https://doi.org/10.5120/ijca2015907704

Leese, J. A., Novak, C. S., & Clark, B. B. (1971). An automated technique for obtaining cloud motion from geosynchronous satellite data using cross correlation. *Journal of Applied Meteorology*, *10*(1), 118–132. https://doi.org/10.1175/1520-0450(1971)010<0118:AATFOC>2.0.CO;2

Li, F., Wang, & Guan (2009). Two methods for cloud motion vectors and its comparative applications in the analysis of typhoon track. *Scientia Meteorologica Sinica*, *29*(3), 330–334.

Liu, K. K. (2015). Study on the characteristics of irregularity occurrence in low-latitude ionosphere *F* region of China. (Doctoral dissertation, University of Chinese Academy of Sciences).

Liu, Z., & Liu, H. (2003). Automatic location of typhoon center using cloud derived wind vectors. *Acta Meteorologica Sinica*, *61*(5), 636–640.

Makela, J. J. (2006). A review of imaging low-latitude ionospheric irregularity processes. *Journal of Atmospheric and Solar-Terrestrial Physics*, *68*(13), 1441–1458. https://doi.org/10.1016/j.jastp.2005.04.014

Martinis, C., & Mendillo, M. (2007). Equatorial spread *F*-related airglow depletions at Arecibo and conjugate observations. *Journal of Geophysical Research*, *112*, A10310. https://doi.org/10.1029/2007JA012403

Mendillo, M., & Baumgardner, J. (1982). Airglow characteristics of equatorial plasma depletions. *Journal of Geophysical Research*, *87*(A9), 7641–7652. https://doi.org/10.1029/JA087iA09p07641

Mukherjee, G. K., Carlo, L., Mahajan, S. H., & Patil, P. T. (1998). First results of all-sky imaging from India. *Earth, Planets and Space*, *50*(2), 119–127. https://doi.org/10.1186/BF03352093

Ning, B. Q., Lianhuan, H. U., Guozhu, L. I., Liu, L. B., & Wan, W. X. (2012). The first time observations of low-latitude ionospheric irregularities by VHF radar in Hainan. *SCIENCE CHINA Technological Sciences*, *55*(5), 1189–1197. https://doi.org/10.1007/s11431-012-4800-2

Nishioka, M., Saito, A., & Tsugawa, T. (2008). Occurrence characteristics of plasma bubble derived from global ground-based GPS receiver networks. *Journal of Geophysical Research*, *113*, A05301. https://doi.org/10.1029/2007JA012605

Ogawa, T., Sagawa, E., Otsuka, Y., Shiokawa, K., Immel, T. I., Mende, S. B., & Wilkinson, P. (2005). Simultaneous ground- and satellite-based airglow observations of geomagnetic conjugate plasma bubbles in the equatorial anomaly. *Earth, Planets and Space*, *57*(5), 385–392. https://doi.org/10.1186/BF03351822

Paulino, I., Medeiros, A. F. D., Buriti, R. A., Takahashi, H., Sobral, J. H. A., & Gobbi, D. (2011). Plasma bubble zonal drift characteristics observed by airglow images over Brazilian tropical region. *Revista Brasileira De Geofísica*, *29*(2), 239–246. https://doi.org/10.1590/S0102-261X2011000200003

Pimenta, A. A., Fagundes, P. R., Bittencourt, J. A., & Sahai, Y. (2001). Relevant aspects of equatorial plasma bubbles under different solar activity conditions. *Advances in Space Research*, *27*(6-7), 1213–1218. https://doi.org/10.1016/S0273-1177(01)00200-9

Pimenta, A. A., Fagundes, P. R., Bittencourt, J. A., Sahai, Y., Gobbi, D., Medeiros, A. F., et al. (2001). Ionospheric plasma bubble zonal drift: A methodology using OI 630 nm all-sky imaging systems. *Advances in Space Research*, *27*(6–7), 1219–1224. https://doi.org/10.1016/S0273-1177(01)00201-0

Sahai, Y., Aarons, J., Mendillo, M., Baumgardner, J., Bittencourt, J. A., & Takahashi, H. (1994). OI 630 nm imaging observations of equatorial plasma depletions at 16°S dip latitude. *Journal of Atmospheric and Terrestrial Physics*, *56*(11), 1461–1475. https://doi.org/10.1016/0021-9169(94)90113-9

Sahai, Y., Fagundes, P. R., & Bittencourt, J. A. (2000). Transequatorial *F*-region ionospheric plasma bubbles: Solar cycle effects. *Journal of Atmospheric and Solar-Terrestrial Physics*, *62*(15), 1377–1383. https://doi.org/10.1016/S1364-6826(00)00179-6

Sekar, R., Chakrabarty, D., Narayanan, R., Sripathi, S., Patra, A. K., & Subbarao, K. S. V. (2004). Analysis of the seasonal variations of equatorial plasma bubble occurrence observed from Haleakala, Hawaii. *Annales Geophysicae*, *22*(9), 3109–3121.

Sharma, A. K., Nade, D. P., Nikte, S. S., Ghodpage, R. N., Patil, P. T., Rokade, M. V., et al. (2012). Analysis of plasma bubbles observed in night airglow emission line OI 630.0 nm from Kolhapur using all sky imager. *International Journal of Engineering Sciences Research*, *03*(02), 746–750.

Sultan, P. J. (1996). Linear theory and modeling of the Rayleigh-Taylor instability leading to the occurrence of equatorial spread *F*. *Journal of Geophysical Research*, *101*(A12), 26875–26891. https://doi.org/10.1029/96JA00682

Tsunoda, R. T. (1985). Control of the seasonal and longitudinal occurrence of equatorial scintillations by longitudinal gradient in integrated *E* region Pedersen conductivity. *Journal of Geophysical Research*, *90*(A1), 447–456. https://doi.org/10.1029/JA090iA01p00447

Weber, E. J., Brinton, H. C., Buchau, J., & Moore, J. G. (1982). Coordinated airborne and satellite measurements of equatorial plasma depletions. *Journal of Geophysical Research*, *87*(A12), 10,503–10,513. https://doi.org/10.1029/JA087iA12p10503

Weber, E. J., Buchau, J., Eather, R. H., & Mende, S. B. (1978). North–south aligned equatorial airglow depletions. *Journal of Geophysical Research*, *83*(A2), 712–716.

Yang, P. L., Liu, X. Y., Guo, F. C., Peng, X. W., Huang, S. X., & Xiang, J. (2013). The preliminary research on cloud motion wind (in chinese). *Mathematics in Practice & Theory*, *27*(6-7), 163–174.

Zhao, S. J., Xiao Yong, S. U., Sun, X. J., Liu, L., & Gao, T. C. (2012). Progress of technology of cloud motion winds by ground-based infrared cloud image. *Journal of Atmospheric Environment Optics*.